Monte Carlo simulation of flexible trimers: From square well chains to amphiphilic primitive models

Guadalupe Jiménez-Serratos, Alejandro Gil-Villegas, Carlos Vega, and Felipe J. Blas

Citation: J. Chem. Phys. **139**, 114901 (2013); doi: 10.1063/1.4820530
View online: http://dx.doi.org/10.1063/1.4820530
View Table of Contents: http://jcp.aip.org/resource/1/JCPSA6/v139/i11
Published by the AIP Publishing LLC.

Monte Carlo simulation of flexible trimers: From square well chains to amphiphilic primitive models

Guadalupe Jiménez-Serratos,[1] Alejandro Gil-Villegas,[1,a)] Carlos Vega,[2] and Felipe J. Blas[3]

[1]*Departamento de Ingeniería Física, División de Ciencias e Ingenierías Campus León, Universidad de Guanajuato, Colonia Lomas del Campestre, León 37150, Mexico*
[2]*Departamento de Química Física, Facultad de Ciencias Químicas, Universidad Complutense de Madrid, Ciudad Universitaria 28040 Madrid, Spain*
[3]*Departamento de Física Aplicada, and Centro de Física Teórica y Matemática FIMAT, Universidad de Huelva, 21071 Huelva, Spain*

(Received 19 June 2013; accepted 23 August 2013; published online 17 September 2013)

In this work, we present Monte Carlo computer simulation results of a primitive model of self-assembling system based on a flexible 3-mer chain interacting via square-well interactions. The effect of switching off the attractive interaction in an extreme sphere is analyzed, since the anisotropy in the molecular potential promotes self-organization. Before addressing studies on self-organization it is necessary to know the vapor liquid equilibrium of the system to avoid to confuse self-organization with phase separation. The range of the attractive potential of the model, λ, is kept constant and equal to 1.5σ, where σ is the diameter of a monomer sphere, while the attractive interaction in one of the monomers was gradually turned off until a pure hard body interaction was obtained. We present the vapor-liquid coexistence curves for the different models studied, their critical properties, and the comparison with the SAFT-VR theory prediction [A. Gil-Villegas, A. Galindo, P. J. Whitehead, S. J. Mills, G. Jackson, and A. N. Burgess, J. Chem. Phys. **106**, 4168 (1997)]. Evidence of self-assembly for this system is discussed. © *2013 AIP Publishing LLC*. [http://dx.doi.org/10.1063/1.4820530]

I. INTRODUCTION

New trends in complex fluids and material sciences require the study of electrolytes, colloids, polymers, liquid crystals, lipid molecules, and in general, any kind of self-assembling systems.[1–9] Computer simulation studies of such systems offer a wide variety of models, techniques, and specific concerns. Monte Carlo and molecular dynamics are used to study models that include atomic or coarse-grain molecular models, lattice or off-lattice treatments, and explicit or implicit solvent simulations, all of them complementing each other to understand their thermodynamic behavior.[1,4,10–16]

Idealized chain fluids, such as long or short chains with hard-body, square-well or Lennard-Jones interactions, have been of interest over the years to model elongated and flexible molecules like polymers or amphiphiles.[4,17–29] These simplified molecular models offer the possibility of understanding the effects of molecular size, shape, and potential on thermodynamic properties, and comparison between theory and simulation results is straightforward. In a different perspective, simplified potential systems have been used to model colloidal self-assembly, following an approach that scales molecular models into real colloidal systems.[30] For example, systems formed by hard-core particles with patch-patch interactions are able to reduce the gas-liquid coexistence, with the consequent presence of regions of intermediate densities where there is not a driving force to induce phase separations.[31,32] These systems can describe colloidal networks analogous to hydrogen-bonded liquid networks.[33] Colloidal particles at the air-water interface also present different structural arrangements like stripes, voids, foams, and chain formation that can be modeled by computer simulation with continuous or discrete-potential systems.[34–36] Janus colloidal particles,[37–39] where two opposite chemical functionalities are attached to the same particle introducing strong competing effects and inducing novel phases, have received a considerable amount of interest due to their wide range of applications[40] and have been studied in relation to their micellization process.[41]

In this work, we study a primitive model of self-assembling discrete-potential system in order to understand its phase diagram. The model is a 3-mer flexible chain interacting via SW potentials and one of the interactions can be tuned to enhance the repulsive interaction in one extreme of the molecule. Simulations were performed with the Metropolis Monte Carlo scheme; direct coexistence simulations in the canonical ensemble (NVT) was obtained in order to study the phase diagram behavior. The attractive interaction in one of the monomers was gradually turned off until a pure hard-body interaction was obtained. This variation introduced a progressive asymmetry in the chain, which can be used to model polymer blends or amphiphilic molecules. In particular, one of the cases analyzed here is similar to amphiphilic models studied by other authors.[12,22–29,42] In such a case, micellar formation can be confused with macroscopic phase

a)Email: gil@fisica.ugto.mx

separation,[42–45] and a systematic study of specific properties is necessary to correctly identify phase diagram regions. The aim of this work is to quantify the effect of the variable-ranged potential on the phase diagram and other properties like the surface tension, as well as the gradual induction of self-assembling behavior as the molecular asymmetry in the interactions is increased. In Sec. II, details of the model and simulation are given; results and discussion are presented in Sec. III; and conclusions are presented in Sec. IV.

II. SIMULATION MODEL AND METHODOLOGY

A. Model

The molecular model consisted of fully flexible chains formed by three tangential monomers. It is helpful to represent the chain with the common notation for amphiphilic models T_2H, i.e., two beads labeled as "tail" and one bead in the extreme as "head". Interactions between monomers are described by three SW potentials: tail-tail (tt), head-head (hh), and head-tail (ht), with form

$$u_{mm}^{SW}(r) = \begin{cases} \infty & \text{for } r \le \sigma \\ -\epsilon_{mm} & \text{for } \sigma < r \le \lambda\sigma, \\ 0 & \text{for } r > \lambda\sigma \end{cases} \quad (1)$$

where m denotes the monomer type (t or h), λ is the potential width, fixed to 1.5 for all cases, and ϵ_{mm} is the depth potential for m-m pairs, given by

$$\begin{aligned} \epsilon_{tt} &= 1.0 && \text{for tail-tail interactions,} \\ \epsilon_{hh} &= K && \text{for head-head interactions,} \\ \epsilon_{ht} &= \sqrt{K} && \text{for head-tail interactions,} \end{aligned}$$

where K takes values between 0 and 1 to control the head-head interaction energy, and the cross-interactions were obtained with the Lorentz-Berthelot combining rules.[46] There is only one intra-molecular interaction that corresponds to the potential between monomers of the same chain separated for more than one junction.

Thermodynamic properties were obtained for independent systems characterized by head-head interaction parameter, K. Studied cases were: $K = 1.0$, 0.7, 0.5, 0.3, 0.1, and 0.0. The case $K = 1.0$ corresponds to a symmetric chain, which is the usual SW trimer model (then there is not distinction between head and tail segments), whereas other values of K introduce an asymmetry between segments.

B. Simulation details

Liquid-vapor coexistence properties were studied by direct coexistence simulations in the canonical ensemble (MC-NVT) using standard moves for displacement, flipping (i.e., exchanging the head monomer with the tail monomer located at the extreme of the chain), rigid body rotation, and relatives displacements between monomers of the same chain, chosen in a random way. Two types of displacements were considered. The first one was a short displacement with an acceptance ratio of 30% –40%, and the second one a long displacement with a smaller acceptance ratio of the order of 5%. The proportion used was 80% for short and 20% for long displacements. The reason to introduce the second type of displacement was to ensure that molecules could migrate to the vapor phase. One MC-NVT cycle is defined as N trial moves. Thermodynamic properties are reported in reduced units: temperature $T^* = k_BT/\epsilon$; density $\rho^* = \rho\sigma^3 = (N/V)\sigma^3$, where σ is the monomer diameter, N is the number of chains in the system, and V the volume of the simulation cell; pressure $P^* = P\sigma^3/\epsilon$; and surface tension $\gamma^* = \gamma\sigma^2/\epsilon$. The simulation box lengths are scaled as $L_i^* = L_i/L_x$ for $i = x, y, z$.

An elongated simulation cell was used with dimensions $L_x^* \times L_y^* \times L_z^* = 1 \times 1 \times 8$, with $L_x \approx 12\sigma$ and $N = 1152$ chains. The initial lattice was a compact arrangement of 8 square slabs of molecules centered at the simulation cell, leaving free space at each side of the arrangement in the z-direction, so that the total density was given by $\rho^* = 0.0738$. Molecules were initially aligned along the z axis. The results for the $K = 0$ system were obtained in a simulation cell with $L_x^* \times L_y^* \times L_z^* = 1 \times 1 \times 12$ and $\rho^* = 0.0490$.

After some initial tests, a temperature was selected to generate a coexistence configuration for the symmetric system $K = 1.0$. The initial lattice was disordered after 10^5 MC-NVT cycles at temperature $T^* = 1.3$. After 5×10^5 cycles, an equilibrated liquid-vapor (L-V) configuration was obtained. This was taken as the initial configuration for simulating the system at a higher temperature, $T^* = 1.35$, and at a lower temperature, $T^* = 1.25$. This process was repeated in order to cover several temperatures under the L-V coexistence region. The equilibrated $K = 1$ configuration at $T^* = 1.3$ was used as initial configuration for systems with $K \neq 1$ and the same procedure was applied to those cases.

Some snapshots for equilibrated states are given in Figure 1, each line is related to a K value and the columns correspond to reduced temperatures. Density profiles were calculated every MC cycle as a function of the long side of the box, $z^* = z/L_x$.

To obtain vapor pressures we performed Monte Carlo simulations in the isothermic-isobaric ensemble (MC-NPT). A small cubic simulation box with $N = 256$ molecules was used and the simulations were performed at very low values of pressure ($P^* \sim 10^{-2}$–10^{-3}). Simulations required 1–5 $\times 10^6$ cycles to equilibrate and 10^6 cycles to obtain averaged properties. In Sec. II D, we detail the calculation of the vapor and critical pressures from these NPT simulations.

A virtual volume perturbation was performed every NVT simulation cycle to obtain the pressure tensor and surface tension. To improve the statistical analysis, averages of pressure components were calculated after 64×10^6 configurations, divided in 8 independent simulations. As described in a previous work,[47] a single volume perturbation parameter ξ ($=\Delta V/V$) is enough for simulating discontinuous potentials; we selected ξ in such a way than around 30%–50% of our volume perturbation trials had a hard body overlap.

C. Density profiles

Profiles were obtained for monomers and molecules as a function of the long side of the simulation box, and

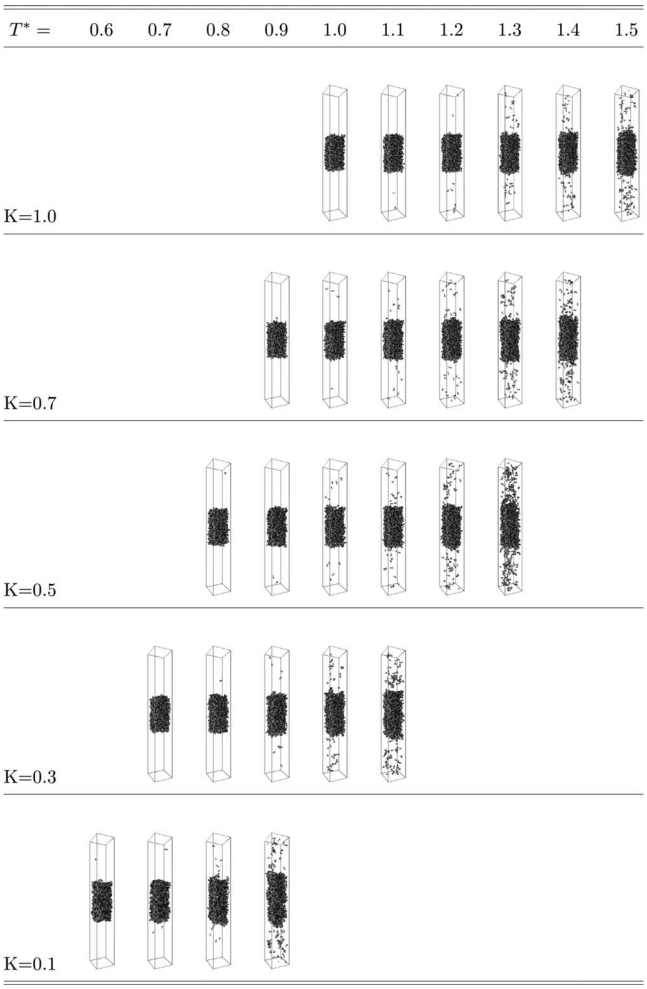

FIG. 1. Snapshots for coexistence configurations of the SW chains system, varying the potential parameter from $K = 1.0$ to $K = 0.1$ and varying temperature. The effect of increasing the temperature can be seen for each system along a row, while the effect of decreasing the K parameter can be seen from up to down for a fixed temperature.

parametrized using an hyperbolic tangent function,[48]

$$\rho^*(z^*) = \frac{1}{2}(\rho_l^* + \rho_v^*) - \frac{1}{2}(\rho_l^* - \rho_v^*)\tanh\left(\frac{z^* - z_0^*}{d^*}\right), \quad (2)$$

where ρ_l^* and ρ_v^* are the bulk densities corresponding to the liquid and vapor phases in coexistence, respectively, $d^* = d/\sigma$ is related to the 10–90 thickness t as $t = 2.19d$ and z_0^* is the position of the transition layer. From this formula, the coexistence densities were obtained in order to generate the orthobaric curve for each system.

D. Vapor pressure

From direct coexistence MC-NVT simulations, we obtained the vapor density $\rho_{v,a}^*$ that corresponds to a given temperature T_a^*. Using this data, the vapor pressure $P_{v,a}^*$ was determined from MC simulations in the isothermic-isobaric ensemble (MC-NPT) of a gas phase in the bulk, according to the following procedure: (i) Three independent NPT simulations were generated varying the pressure P_i^* (where $i = 1, 2, 3$) taking values near to the vapor density $\rho_{v,a}$, assuming an ideal gas behavior, and keeping a constant temperature T_a^*, (ii) Once equilibrium densities $\rho_{eq,i}^*$ were obtained, the set of values $(\rho_{eq,i}^*, P_i^*)$ were fitted using a linear equation; (iii) Using the actual vapor density $\rho_{v,a}^*$ in the linear equation, an accurate estimation of the vapor pressure $P_v^* = P_{v,a}^*$ was obtained.

A complementary method to estimate P_v^* can be used by evaluating the pressure tensor applying the virtual-volume perturbation MC method (VP), as we explain in Sec. II F.

E. Critical points

The vapor and liquid densities obtained from Eq. (2) were used to generate the L-V coexistence curve of the systems, and then to estimate the critical temperature T_c^* using the standard scaling relationship,

$$\rho_l^* - \rho_v^* = A(T_c^* - T^*)^\beta, \quad (3)$$

where A is a constant and β is the critical exponent, for which a value of $\beta = 1/3$ was assumed. The rectilinear diameter formula

$$\frac{\rho_l^* + \rho_v^*}{2} = B + CT^* \quad (4)$$

was applied using the coexistence densities of every system, where constants B and C were determined by linear regression. With the critical temperature T_c^* an estimation of the critical density ρ_c^* was obtained. By combining Eqs. (3) and (4) for the vapor and liquid densities, the coexistence curve can be fitted for each branch, ρ_v^* and ρ_l^*.

On the other hand, the critical pressure was calculated by fitting the vapor pressure data to the Clausius-Clapeyron equation,[46]

$$\ln P^* = a + \frac{c}{T^*}, \quad (5)$$

and using T_c^*. In this case, an accurate determination of constants a and b requires to consider the independent errors for each P_v^* value as weights in the fitting procedure.[49]

F. Surface tension

The surface tension can be written in terms of the macroscopic normal P_N and tangential P_T pressure components,[50–52]

$$\gamma = \frac{1}{2}L_z[P_N - P_T], \quad (6)$$

where the factor 2 takes into account the two interfaces of the simulation box.

For the systems in coexistence, the interface is contained in the $x - y$ plane which is isotropic. Then, the tangential component is given by $P_T = (p_{xx}^* + p_{yy}^*)/2$, whereas the normal component is $P_N = p_{zz}^*$. In the gas region, P_N is constant and can be identified with the vapor pressure, $P_v^* = P_N$.

In order to study the effect of the potential parameter K in the interfacial properties, the surface tension is obtained from Eq. (6) and the pressure components were calculated from MC-NVT simulations, applying the virtual volume perturbation method (VP). In the case of discontinuous potentials, and for non-spherical models, as our chains, some difficulties appear in the implementation of the VP method. Following

the method presented in our previous work,[47] the pressure is given by

$$p = p_{ideal} + p_{-}^{(HB+SW)} + p_{+}^{(HB)}. \quad (7)$$

The ideal contribution is $p_{ideal} = Nk_BT/V_i$, being V_i the unperturbed volume of the NVT box. The second term corresponds to a compression contribution, denoted by the minus sign,

$$p_{-}^{(HB+SW)} = \lim_{\Delta V_{i\to j-}\to 0} \frac{k_BT}{\Delta V_{i\to j-}} \ln\left\langle \exp\left(-\frac{\Delta U_{i\to j-}^{(HB+SW)}}{k_BT}\right)\right\rangle_{eq}. \quad (8)$$

The subscript j indicates a virtual state, obtained by perturbing the volume from V_i to V_j, so that $\Delta V_{i\to j-}$ is the volume change and $\Delta U_{i\to j-}^{(HB+SW)}$ is the energy difference between i and j states. In this case, the label HB+SW emphasizes that the complete potential is taken into account. The third term in Eq. (7) corresponds to an expansion contribution, denoted by a plus sign,

$$p_{+}^{(HB)} = \lim_{\Delta V_{i\to j+}\to 0} \frac{k_BT}{\Delta V_{i\to j+}} \ln\left\langle \exp\left(-\frac{\Delta U_{i\to j+}^{(HB)}}{k_BT}\right)\right\rangle_{eq}. \quad (9)$$

Here, the notation is similar to the compression equation, but in this case only the HB interaction is taken into account. So, when a virtual volume expansion is performed, there are contributions only from the few cases in which an HB overlapping configuration is produced, as was shown by Brumby *et al.* for non-spherical molecules.[52]

To evaluate the components of the pressure tensor, an anisotropic virtual change in volume is applied. If the component to calculate is $p_{\alpha\alpha}$, for $\alpha = x$, y, or z, then the simulation box changes only its α size from L_α to $L_\alpha + \Delta L_\alpha$. Finally, we define a volume perturbation parameter as $\xi = \Delta V/V$, for the anisotropic case it is given by $\xi = \Delta L_\alpha/L_\alpha$.

III. RESULTS AND DISCUSSION

A. $K \neq 0$ systems

Density profiles were calculated in the MC-NVT simulations for each one of the monomers in the chain model. Although the density profiles are the same for the three monomers when far from gas-liquid interface, near to the interface, the individual density profiles are somewhat different. In Figure 2, the density profile for each individual monomer for $K = 0.3$ and $T^* = 0.9$ is plotted. As it can be seen in this figure, the head monomer is absorbed preferentially at the liquid-vapor interface. This is reflected in the fact that its density profile is the last to decay to the gas density. This is a consequence of the asymmetry of the chain. The same results is obtained for other values of K although the preferential absorption of the head monomer is not so pronounced when increasing the value of K. In the rest of this work, we shall present the density profiles as averaged over the three monomers. Once the density profiles for subcritical temperatures were obtained, they were fitted to an hyperbolic tangent function, Eq. (2). The numerical results for the vapor density,

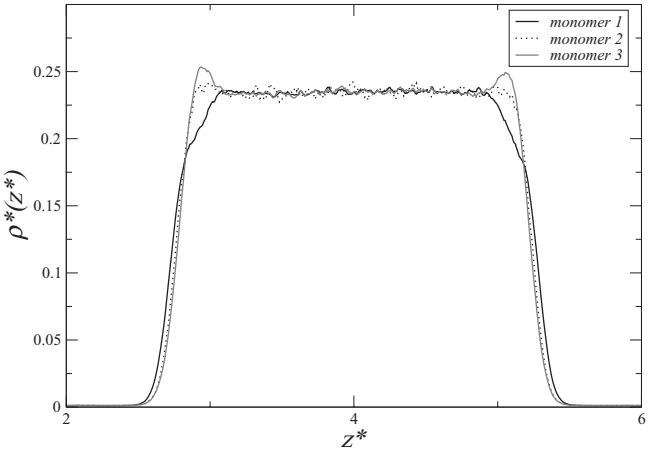

FIG. 2. Detail of the individual density profiles, calculated for the three monomers, as a function of the major axis of the simulation cell in reduced units, z^*. *Monomer 1* is the head, *monomer 2* is the central bead, and *monomer 3* is the extreme monomer of the tail. The curves correspond to the $K = 0.3$ system at temperature $T^* = 0.9$ and show how the individual profiles discern between sites for low K values and low temperatures.

liquid density, and interface width obtained from the fit are given in Tables I–V.

The effect of the potential parameter in the density profile is presented in Figure 3 for $T^* = 1.0$ and $K = 1.0$, 0.7, 0.5, and 0.3. As K decreases it is easier for the molecules to migrate to the gas phase, and lower values of K cause larger values of the vapor density. This effect can also be seen in Figure 4 that presents the liquid-vapor coexistence curves for different systems. The continuous line is the result given by Eqs. (3) and (4), the corresponding critical points are indicated. The effect of the potential parameter in the coexistence curves is appreciable, particularly for small values of K. Again, as K decreases, a lower energy is needed by the chains to separate each other, so the critical temperature also decreases. The effect in the critical density is not perceptible for large values of K, but there is a change for the critical density at low K. Critical points were more difficult to estimate at low K, due to larger uncertainties in ρ^* and T^*. The critical densities and temperatures obtained from simulations and theory are given in Table VI. In the case $K = 1$, we can reproduce the reported data in Ref. 19 for the same model.

The simulation results for the liquid-vapor (L-V) coexistence curves for $K = 1.0$, 0.5, and 0.1 are given in Figure 5 and compared with the theoretical predictions obtained from the Associating Fluid Theory for potentials of variable range (SAFT-VR).[53,54] The theoretical curve for $K = 0.0$ is also given. The SAFT-VR approach is based on the Wertheim';s thermodynamic perturbation theory[55] for fluids with anisotropic interactions. Detailed information about the SAFT-VR's Helmholtz free energy A for a fluid formed by N chain molecules is given in the Appendix and in Refs. 53, 54, and 56–59.

Results are accurate for systems at temperatures far from the critical point, which is overestimated by around 10% respect to the simulation value. The SAFT-VR prediction deteriorates for $K = 0.1$; a possible explanation for this effect is that Wertheim theory requires to evaluate the chain energy using the radial distribution function of the monomeric

TABLE I. Coexistence properties for the system of flexible SW trimers with potential parameter $K = 1.0$. The data were obtained from direct liquid-vapor coexistence MC-NVT simulations at fixed density $\rho^* = 0.0738$ and subcritical temperatures. For each isotherm we report: vapor density ρ_v^*, liquid density ρ_l^*, interface width d^*, and vapor pressure P_v^*, which was obtained from independent MC-NPT simulations.

T^*	T^*/T_c^*	ρ_v^*	ρ_l^*	d^*	P_v^*
1.10	0.604	$1.5(5) \times 10^{-4}$	0.253(1)	0.940(5)	$1.6(6) \times 10^{-4}$
1.15	0.631	$3.4(5) \times 10^{-4}$	0.248(1)	1.009(5)	$3.8(7) \times 10^{-4}$
1.20	0.659	$6.7(5) \times 10^{-4}$	0.2432(8)	1.148(4)	$7.8(8) \times 10^{-4}$
1.25	0.686	$1.09(8) \times 10^{-3}$	0.2392(7)	1.180(3)	$1.3(1) \times 10^{-3}$
1.30	0.714	$1.78(4) \times 10^{-3}$	0.2338(3)	1.229(3)	$2.2(1) \times 10^{-3}$
1.35	0.741	$2.63(3) \times 10^{-3}$	0.228(1)	1.668(5)	$3.2(1) \times 10^{-3}$
1.40	0.769	$4.1(1) \times 10^{-3}$	0.2218(5)	1.597(4)	$4.9(2) \times 10^{-3}$
1.45	0.796	$6.1(2) \times 10^{-3}$	0.216(2)	1.689(4)	$7.2(3) \times 10^{-3}$
1.50	0.823	$9.1(1) \times 10^{-3}$	0.207(9)	1.915(4)	$1.07(9) \times 10^{-2}$
1.55	0.851	$1.22(1) \times 10^{-2}$	0.198(2)	2.836(5)	$1.4(1) \times 10^{-2}$

fluid of the bonding species. In our case, there are two bonds: SW-SW and SW-HS, and then the radial distribution function of the corresponding mixtures are used. However, by computer simulation we found that an equimolar binary mixture of hard spheres and square-well particles is immiscible at low temperatures; the radial distribution function obtained from an hypothetical miscible HS-SW mixture is very different from the immiscible one and this effect suggests that we should be modeling the chain contribution to the free energy with the value of the radial distribution function of the actual mixture.

As was described in Sec. II D, vapor pressures were calculated from MC-NPT simulations and a parametric formula. The results for each system and temperature appear in the last column of Tables I–V. The corresponding graphic in logarithmic scale is given in Figure 6, where the continuous line is the fitted curve of the data to Eq. (5). This linear behavior allows us to predict the critical value for the pressure, which is also given in the Figure 6.

Vapor pressures have been compared with SAFT-VR results, some of the cases are given in Figure 7. It was found that the theoretical prediction of the curve is in agreement with the simulation data, even for low values of K. The prediction of the critical pressure requires to know T_c, so, it is also sensitive to the accuracy of the previously fitted expressions. We found a good agreement between simulation and theory for the critical pressure at large values of K, but the prediction deteriorates as K is reduced.

In Table VI, we give the critical pressure obtained from simulation and from SAFT-VR approach. The critical pressure decreases by lowering K, as a consequence of the reduction of the attractive interactions.

Finally, we present results for the surface tension for some states of different K systems. The numerical values are given in Table VII; the second and third columns correspond to the reduced temperatures T^* and T^*/T_c^*; the fourth and fifth columns are the tangential and normal values for pressure calculated from MC-NVT simulations applying the volume perturbation method;[47] the sixth column is the pressure vapor obtained from MC-NPT simulations (also given in Tables I–V); and the last two columns correspond to the surface tension calculated with Eq. (6) using as normal pressure: (1) the z-component of the pressure calculated via the VP method, $P_N^* = p_{zz}^*$ and (2) the vapor pressure, $P_N^* = P_v^*$. For pressure values around 10^{-4}, the error bar in the normal pressure component is of the same order of magnitude as the vapor pressure itself. For this reason, it is better to obtain the normal pressure component from the simulations of the gas phase that reproduce the gas density obtained in the direct coexistence simulations. We shall now describe the qualitative

TABLE II. Coexistence properties for the system of flexible SW trimers with potential parameter $K = 0.7$. The data were obtained from direct liquid-vapor coexistence MC-NVT simulations at fixed density $\rho^* = 0.0738$ and subcritical temperatures. For each isotherm we report: vapor density ρ_v^*, liquid density ρ_l^*, interface width d^*, and vapor pressure P_v^*, which was obtained from independent MC-NPT simulations.

T^*	T^*/T_c^*	ρ_v^*	ρ_l^*	d^*	P_v^*
1.00	0.618	$2.1(3) \times 10^{-4}$	0.2515(2)	0.971(4)	$2.1(3) \times 10^{-4}$
1.05	0.649	$5.3(9) \times 10^{-4}$	0.2457(2)	1.098(3)	$5(1) \times 10^{-4}$
1.10	0.680	$9.3(9) \times 10^{-4}$	0.2404(6)	1.209(4)	$1.0(1) \times 10^{-3}$
1.15	0.711	$1.56(3) \times 10^{-3}$	0.2336(6)	1.204(3)	$1.68(5) \times 10^{-3}$
1.20	0.742	$2.68(6) \times 10^{-3}$	0.226(2)	1.340(5)	$2.9(2) \times 10^{-3}$
1.25	0.773	$4.1(1) \times 10^{-3}$	0.221(2)	1.594(4)	$4.4(2) \times 10^{-3}$
1.30	0.804	$6.2(4) \times 10^{-3}$	0.213(3)	1.834(7)	$6.6(5) \times 10^{-3}$
1.35	0.835	$9.6(2) \times 10^{-3}$	0.2012(5)	2.06(1)	$1.00(3) \times 10^{-2}$
1.40	0.865	$1.39(7) \times 10^{-2}$	0.194(8)	2.33(2)	$1.4(1) \times 10^{-2}$

TABLE III. Coexistence properties for the system of flexible SW trimers with potential parameter $K = 0.5$. The data were obtained from direct liquid-vapor coexistence MC-NVT simulations at fixed density $\rho^* = 0.0738$ and subcritical temperatures. For each isotherm we report: vapor density ρ_v^*, liquid density ρ_l^*, interface width d^*, and vapor pressure P_v^*, which was obtained from independent MC-NPT simulations.

T^*	T^*/T_c^*	ρ_v^*	ρ_l^*	d^*	P_v^*
0.90	0.630	$2.1(7) \times 10^{-4}$	0.2510(5)	0.986(5)	$1.9(6) \times 10^{-4}$
0.95	0.665	$3.9(5) \times 10^{-4}$	0.2462(5)	0.974(5)	$3.6(5) \times 10^{-4}$
1.00	0.700	$8.9(1) \times 10^{-4}$	0.2401(5)	1.247(5)	$8.5(2) \times 10^{-4}$
1.05	0.735	$1.6(1) \times 10^{-3}$	0.2331(2)	1.286(6)	$1.56(4) \times 10^{-3}$
1.10	0.770	$2.87(9) \times 10^{-3}$	0.2253(2)	1.513(5)	$2.8(1) \times 10^{-3}$
1.15	0.805	$4.9(1) \times 10^{-3}$	0.2144(2)	1.866(8)	$4.7(2) \times 10^{-3}$
1.20	0.840	$7.7(1) \times 10^{-3}$	0.2066(5)	2.034(8)	$7.2(3) \times 10^{-3}$
1.25	0.875	$1.19(1) \times 10^{-2}$	0.192(1)	2.328(9)	$1.0(1) \times 10^{-2}$
1.30	0.910	$1.83(2) \times 10^{-2}$	0.1791(3)	3.028(9)	$1.5(1) \times 10^{-2}$

changes on the surface tension that occurs when changing the parameter K.

As an example, we will take the comparison between systems $K = 1.0$ and $K = 0.5$ given in the Figure 8. The surface tension for systems at the same relative temperature T^*/T_c^* decreases for lower values of K. Then, as the asymmetry in the model is enhanced, chains resemble the surfactant molecules: on the one hand, the chain model and real molecules are composed by two dissimilar parts and, on the other hand, the simulations reproduce the effect of lowering the surface tension, as surfactants do. Also, in this graph we can notice that the studied systems do not follow corresponding states behavior since the change in the interactions introduced by the K values gives non-conformal cases.

B. The $K = 0$ system

Some partial and qualitative results for the system with $K = 0$ are presented. This system corresponds to the completely asymmetric chain model, i.e., a hard sphere and two SW monomers. The methodology used to study the systems with $K \neq 0$ was not adequate to study the $K = 0$ case, since information could not be obtained from the direct coexistence simulations.

From the tendency of the $K \neq 0$ systems, we expected a critical point of about $T^* = 0.75$, i.e., about 10% lower than the estimated of the critical temperature for $K = 0$ obtained from SAFT-VR, which is $T^* = 0.836$. Then simulations were generated below this temperature. It is interesting to observe that the ratio of the critical temperatures $T_c(K = 0)/T_c(K = 1.0) = 0.4207$, which is very close to 4/9, that corresponds to the ratio of the number of SW interactions (4 for the $K = 0$ and 9 for the $K = 1.0$ chains). In Figure 9(a), we give a snapshot of the system at $T^* = 0.66$, obtained from an initial configuration formed by bilayers. These bilayers were deformed by slowly increasing the temperature. If we observe the individual density profiles for each type of monomer, it is confirmed that the system presents structure, even for the more disordered configurations. By decreasing the temperature again, the system presented a supramolecular organization forming bilayers at low temperatures. This is given for the system at $T^* = 0.54$ in Fig. 9(b). A detail of the bilayer located around $z^* = 8.6$ is given in the inset of the density profiles, confirming a clear preferential organization of the asymmetric chains.

Supramolecular organization was expected, since the $K = 0$ trimer and other similar chains with asymmetric interactions have been used in previous works by other authors to model amphiphilic molecules.[5,21–29,42] These effective interactions for implicit solvent models are based on the generally accepted assumption that hydrophobic interaction dominates over other forces between amphiphile beads.[22,28]

The $K = 0$ trimer corresponds to one of the models studied in Ref. 28, in which different types of micellar formations were observed varying λ and ϵ. We were not able to obtain

TABLE IV. Coexistence properties for the system of flexible SW trimers with potential parameter $K = 0.3$. The data were obtained from direct liquid-vapor coexistence MC-NVT simulations at fixed density $\rho^* = 0.0738$ and subcritical temperatures. For each isotherm we report: vapor density ρ_v^*, liquid density ρ_l^*, interface width d^*, and vapor pressure P_v^*, which was obtained from independent MC-NPT simulations.

T^*	T^*/T_c^*	ρ_v^*	ρ_l^*	d^*	P_v^*
0.80	0.635	$1.6(9) \times 10^{-4}$	0.2494(5)	0.946(6)	$1.3(7) \times 10^{-4}$
0.85	0.675	$4.7(1) \times 10^{-4}$	0.2418(5)	1.084(5)	$3.9(1) \times 10^{-4}$
0.90	0.714	$1.0(4) \times 10^{-3}$	0.235(1)	1.237(4)	$9(4) \times 10^{-4}$
0.95	0.754	$2.07(2) \times 10^{-3}$	0.2260(5)	1.336(6)	$1.77(6) \times 10^{-3}$
1.00	0.794	$3.80(1) \times 10^{-3}$	0.217(1)	1.541(6)	$3.2(3) \times 10^{-3}$
1.05	0.833	$6.3(8) \times 10^{-3}$	0.206(2)	1.995(9)	$5.2(7) \times 10^{-3}$
1.10	0.873	$1.1(2) \times 10^{-2}$	0.188(2)	2.04(2)	$8(2) \times 10^{-3}$
1.15	0.913	$1.7(4) \times 10^{-2}$	0.1733(5)	3.19(1)	$1.2(2) \times 10^{-3}$

TABLE V. Coexistence properties for the system of flexible SW trimers with potential parameter $K = 0.1$. The data were obtained from direct liquid-vapor coexistence MC-NVT simulations at fixed density $\rho^* = 0.0738$ and subcritical temperatures. For each isotherm we report: vapor density ρ_v^*, liquid density ρ_l^*, interface width d^*, and vapor pressure P_v^*, which was obtained from independent MC-NPT simulations.

T^*	T^*/T_c^*	ρ_v^*	ρ_l^*	d^*	P_v^*
0.700	0.688	$3(2) \times 10^{-4}$	0.226(5)	1.16(1)	$2(1) \times 10^{-4}$
0.725	0.712	$6(1) \times 10^{-4}$	0.221(4)	1.29(1)	$4.2(9) \times 10^{-4}$
0.750	0.737	$8.8(8) \times 10^{-4}$	0.218(3)	1.32(1)	$6.2(8) \times 10^{-4}$
0.775	0.761	$1.29(2) \times 10^{-3}$	0.209(2)	1.42(2)	$9.1(3) \times 10^{-4}$
0.800	0.786	$1.8(5) \times 10^{-3}$	0.201(6)	1.28(2)	$1.3(3) \times 10^{-3}$
0.825	0.810	$3.0(3) \times 10^{-3}$	0.195(5)	1.76(2)	$2.0(3) \times 10^{-3}$
0.850	0.835	$4(1) \times 10^{-3}$	0.188(6)	2.13(2)	$2.6(6) \times 10^{-3}$
0.875	0.860	$5.6(4) \times 10^{-3}$	0.182(9)	2.47(4)	$3.5(5) \times 10^{-3}$

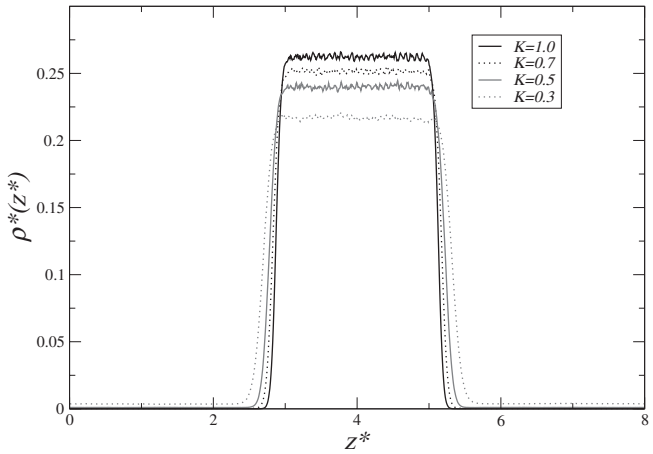

FIG. 3. Density profiles as a function of the major axis of the simulation cell in reduced units, $z^* = z/L_x$. The curves correspond to temperature $T^* = 1.0$ and show the effect of the potential parameter K.

TABLE VI. Critical values for systems of flexible SW trimers with potential parameter K. For each case we give: critical density ρ_c^*, critical temperature T_c^*, and critical pressure P_c^*. The values were obtained from fits to simulation data as described in the text. The second line in each case corresponds to SAFT-VR predictions.

K	ρ_c^*	T_c^*	P_c^*
1.0	0.0932 ± 0.0081	1.822 ± 0.114	0.0665 ± 0.0080
	0.0952	1.987	0.0707
0.7	0.0912 ± 0.0099	1.618 ± 0.116	0.0549 ± 0.0050
	0.0959	1.765	0.0627
0.5	0.0910 ± 0.0098	1.429 ± 0.070	0.0406 ± 0.0030
	0.0960	1.599	0.0561
0.3	0.0871 ± 0.0166	1.260 ± 0.094	0.0371 ± 0.0048
	0.0953	1.401	0.0470
0.1	0.0767 ± 0.0198	1.018 ± 0.097	0.0163 ± 0.0011
	0.0894	1.132	0.0321

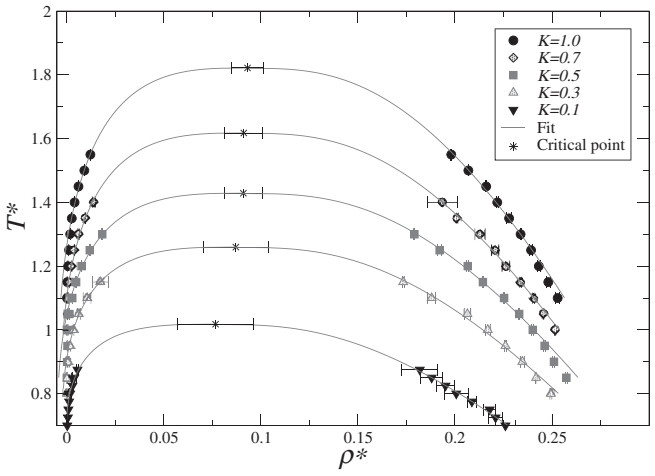

FIG. 4. Liquid-vapor coexistence curves for SW chains systems with potential parameter K. The solid symbols correspond to the data obtained from direct coexistence simulations, this is, liquid and vapor densities that came out from the fit to the simulated density profiles using Eq. (2). The continuous line is the fit calculated from Eqs. (3) and (4), while the asterisks indicate the critical points predicted by these fits for each case. Error bars are also shown for all cases.

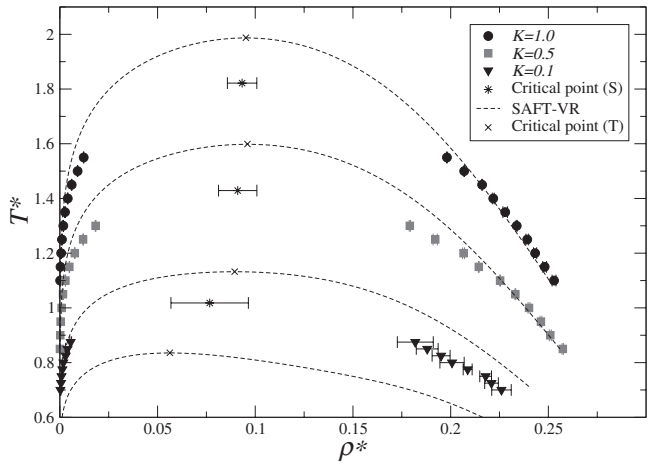

FIG. 5. Comparison between simulation data and SAFT-VR theory for L-V coexistence curves. Simulation results (S) are given for SW chains systems with potential parameter $K = 1.0$, 0.5, and 0.1, while SAFT-VR curves (T) are given for $K = 1.0$, 0.5, 0.1, and 0.0.

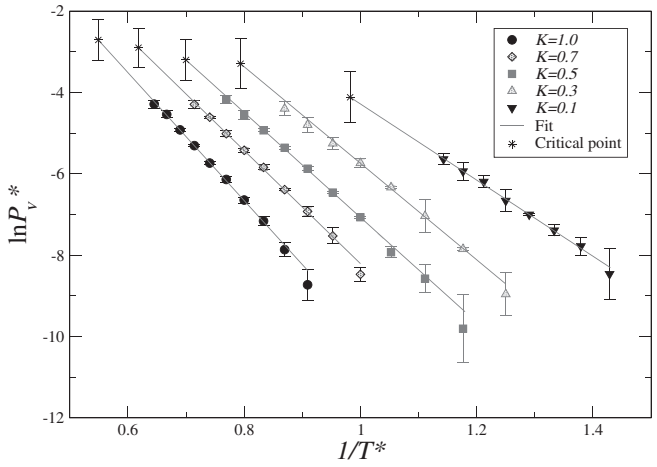

FIG. 6. Vapor pressure in logarithmic scale as a function of the inverse of the temperature $1/T^*$ for SW chains systems with potential parameter K. The solid symbols correspond to values obtained from the linear fit to low-density simulations data, using NPT ensemble. The continuous line is the fit calculated from Eq. (5) weighting errors,[49] while the asterisks indicate the critical points predicted by these fits for each case. Error bars are also given for all cases.

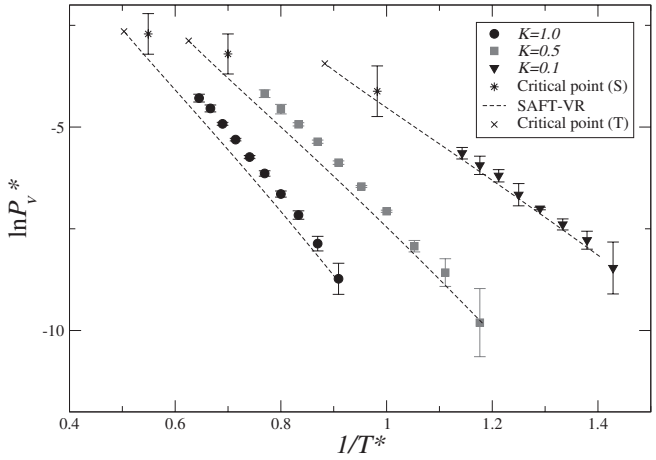

FIG. 7. Comparison between simulation data and SAFT-VR theory for vapor pressure in logarithmic scale as a function of the inverse of the temperature. Results are given for SW chains systems with potential parameter $K = 0.1$, 0.5, and 1.0.

equilibrated configurations of micelles as observed in Ref. 28 for the same simulation conditions, i.e., a cubic simulation cell with $N = 2000$ and $L_x \approx 48\sigma$ that corresponds to $\rho^* \approx 0.018$. Instead, the energy presented a monotonous behavior even after 10^7 cycles and the system exhibited a ramified structure that resembles a gel. In Figure 10, we present a final snapshot and energy per molecule as a function of NVT cycles. The chain is a variation of the $K = 0$ model, changing the SW values to $\lambda = 1.1$ and $T^* = 0.3226$, also studied in Ref. 28. A similar energy drift and configurations have been observed by Sciortino and co-workers in Molecular Dynamics simulations of short-range attractive systems that present gel, glass, and arrested phases.[9,60–62] MC-NVT simulations at lower densities $\rho^* \approx 0.0002$ for a cubic cell resulted in the formation of stable aggregates in the system. As has been studied by Panagiotopoulos and co-workers,[42–45] micellization implies phase separation on a microscopic length scale but not on a macroscopic one. Increasing the system size should give similar aggregation numbers in case of micellization, while aggregation numbers move to infinite in the thermodynamic limit under phase separation.

Qualitative tests of system size effects were performed using NVT ensemble. The NVT simulations were performed at $T^* = 0.6$ for two boxes of different size, maintaining the same density. The resulting configurations and energy behavior are presented in Figure 11 for $\rho^* = 7.06 \times 10^{-4}$. The box on the left side has $N = 256$ trimers, while the box on the right side includes $N = 2048$ chains. Qualitatively, smaller and bigger systems exhibit similar structures. A noisy behavior is exhibited by the energies but the drastic energy drift of Fig. 10(b) is not present. Micellar formation can be observed, although these preliminary tests and their equilibrium must be verified with simulations that include biased-moves techniques to accelerate convergence. Convenient bias moves could be cluster moves and biased moves at low densities.[63,64] To avoid misleading micellization with phase separation in such cases, further techniques must be implemented. On the other hand, the possibility that the liquid phase is pre-empted

TABLE VII. Surface tension calculated from MC-NVT + VP simulations for flexible trimer models with potential parameter K. For the selected temperatures, fourth to sixth columns give the tangential component of the pressure $p_T^* = (1/2)(p_{xx}^* + p^* pyy)$, the pressure component for the major axis of the simulation cell p_{zz}^* and the vapor pressure P_V^*, which was obtained from independent MC-NPT simulations. The last two columns give the surface tension calculated using as normal component p_N^*: (1) the direct VP result for p_{zz}^*, and (2) the vapor pressure P_V^*.

K	T^*	T^*/T_c^*	p_T^*	p_{zz}^*	P_V^*	$\gamma^*(p_N^* = p_{zz}^*)$	$\gamma^*(p_N^* = P_V^*)$
1.0	1.1	0.6038	$-1.24(7) \times 10^{-2}$	$5(7) \times 10^{-4}$	$1.6(6) \times 10^{-4}$	0.64(7)	0.63(4)
	1.2	0.6587	$-8.6(8) \times 10^{-3}$	$2(1) \times 10^{-3}$	$7.8(8) \times 10^{-4}$	0.51(9)	0.47(4)
	1.3	0.7136	$-6.0(8) \times 10^{-3}$	$1.6(7) \times 10^{-3}$	$2.2(1) \times 10^{-3}$	0.38(7)	0.41(4)
	1.4	0.7685	$-4.2(5) \times 10^{-3}$	$3.0(5) \times 10^{-3}$	$1.68(5) \times 10^{-3}$	0.36(5)	0.29(3)
0.7	1.0	0.6182	$-1.03(7) \times 10^{-2}$	$4(5) \times 10^{-4}$	$2.1(3) \times 10^{-4}$	0.53(6)	0.52(4)
	1.15	0.7109	$-4.2(5) \times 10^{-3}$	$3.0(5) \times 10^{-3}$	$1.68(5) \times 10^{-3}$	0.36(5)	0.29(3)
0.5	0.95	0.6649	$-6.1(5) \times 10^{-3}$	$9(4) \times 10^{-4}$	$3.6(5) \times 10^{-4}$	0.35(4)	0.32(3)
	1.05	0.7349	$-3.6(3) \times 10^{-3}$	$2.2(2) \times 10^{-3}$	$1.56(4) \times 10^{-3}$	0.29(3)	0.26(2)
0.3	0.8	0.6350	$-6.2(7) \times 10^{-3}$	$5(6) \times 10^{-4}$	$1.3(7) \times 10^{-4}$	0.33(6)	0.32(4)
	0.9	0.7144	$-4.1(7) \times 10^{-3}$	$1.6(7) \times 10^{-3}$	$9(4) \times 10^{-4}$	0.28(7)	0.25(5)
0.1	0.75	0.7367	$-3(5) \times 10^{-4}$	$1.6(6) \times 10^{-3}$	$6.2(8) \times 10^{-4}$	0.10(5)	0.05(3)

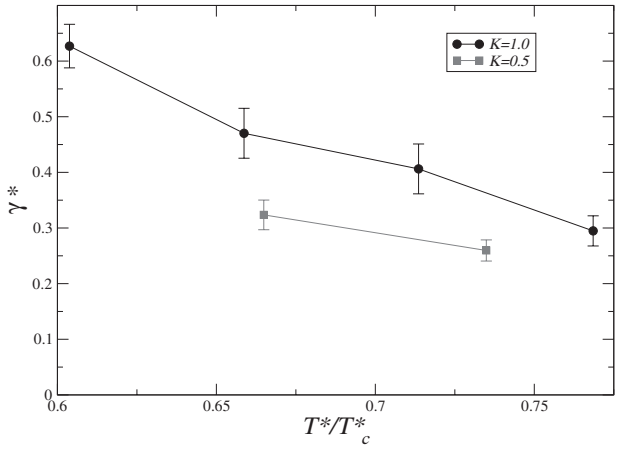

FIG. 8. Surface tension as a function of the scaled temperature T^*/T_c^* for the flexible trimers with potential parameter $K = 1.0$ and 0.5. Solid symbols correspond to the calculated values using $p_N^* = P_v^*$ (last column of Table VII) and the lines are just an eye guide to follow the behavior of the surface tension for each K value.

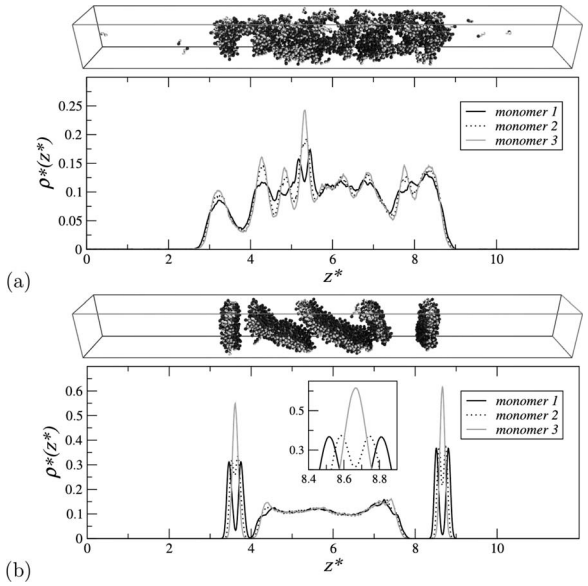

FIG. 9. Equilibrated configuration snapshot and the corresponding density profiles per monomer for trimers with $K = 0$ and $\lambda = 1.5$ at temperatures (a) $T^* = 0.66$ and (b) $T^* = 0.54$. *Monomer 1* is the head, *monomer 2* is the central bead, and *monomer 3* is the extreme monomer of the tail.

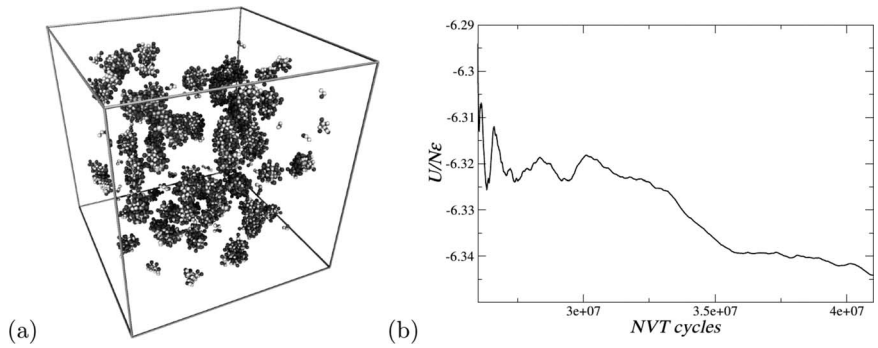

FIG. 10. (a) Snapshot and (b) energy data for a trimer with hard-sphere head and SW tail, $K = 0$ and $\lambda = 1.1$, at temperature $T^* = 0.3226$ and density $\rho^* = 0.018$.

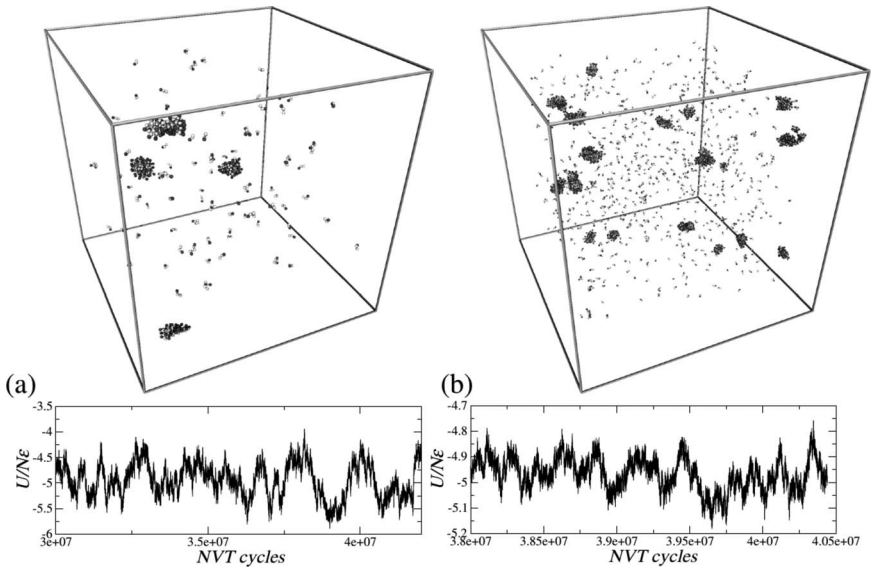

FIG. 11. Snapshots and energy as a function of NVT cycles for trimers with $K = 0$ and $\lambda = 1.5$ at temperature $T^* = 0.6$ and density $\rho^* = 7.06 \times 10^{-4}$ for (a) $N = 256$ molecules and (b) $N = 2048$ molecules.

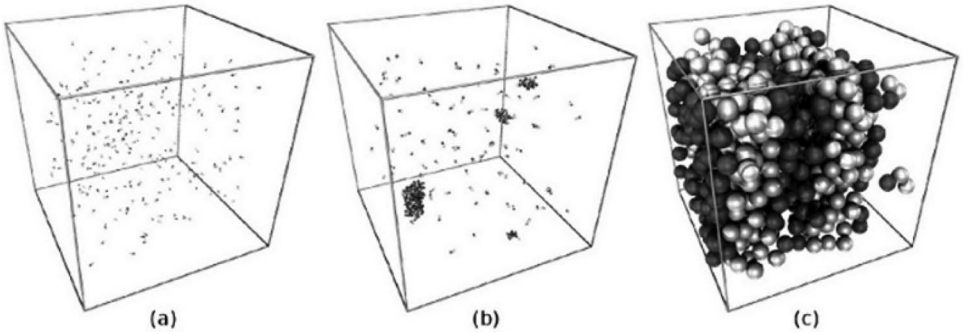

FIG. 12. Snapshots for $N = 256$ trimers with $K = 0$ and $\lambda = 1.5$ at temperature $T^* = 0.6$ and pressures (a) $P^* = 2.7 \times 10^{-4}$; (b) $P^* = 2.85 \times 10^{-4}$; and (c) $P^* = 5.0 \times 10^{-1}$.

by a lamellar phase requires a detailed study; however, in Fig. 12, we present three snapshots for the isotherm $T^* = 0.6$ obtained by NPT simulations for pressures $P^* = 2.7 \times 10^{-4}$, 2.85×10^{-4}, and 5.0×10^{-1}; the corresponding densities are $\rho^* = 2.81 \times 10^{-4}$, 7.06×10^{-4}, and 0.23, respectively. We observe from Fig. 12 that the system evolves from a gas to a micellar phase at low densities, located at the left-hand side of the SAFT-VR LV coexistence curve (see Fig. 5) and then reaches a lamellar phase at higher density, to the right-hand side of the SAFT-VR LV curve.

Interplay of repulsive and attractive ranges can also give place to micellization or phase separation phenomena.[42,65] To identify gel-like phases, micellar formation or phase separation in the $K = 0$ system, a systematic study is required in order to understand the phase diagram.

IV. CONCLUSIONS

Effects of the interactions in the phase diagram were studied for a flexible trimer that was gradually modified from the SW trimer to an amphiphilic model. As the value of the potential parameter K decreased, the critical temperatures and densities were lowered, and the effect became more dramatic for smaller K values. A similar gradual tendency was observed for surface tension calculations, having a lower surface tension the system with smaller K, i.e., the chain more similar to amphiphilic models. These progressive changes are not sustained in a continuous way for the case $K = 0$, that behaved completely different from the other systems. Actually, system with $K = 0.1$ was, qualitatively, more similar to $K = 1.0$ chains than to $K = 0$ system. This case corresponds to chains composed by one monomer with pure hard-body repulsion and two segments with square-well attractive potential. The individual monomers with such interactions would form an immiscible mixture, but in the model are forced to be attached to each other, which promotes self-assembled configurations. Further work is needed in order to characterize those phases and to understand the micellar formation conditions. Calculations of other properties are required to avoid misleading gel-like, arrested, glassy, and micellar phases.[9,42–45,60–62] Finally, the understanding of the phase behavior of the effective model presented here could be proposed as a prototype for colloidal self-assembly, following a recent approach that scales molecular models into real colloidal systems.[30]

ACKNOWLEDGMENTS

We acknowledge financial support from CONACYT (Programa de Becas Mixtas, México), MEC (Spain) through Grant Nos. FIS2010-16159 and FIS2010-14866, Junta de Andalucía, and Universidad de Huelva.

APPENDIX: SAFT-VR

SAFT-VR[53,54] was the theoretical framework used to describe the studied systems in this work. According to this approach, the Helmholtz free energy $a = A/Nk_BT$ is given by

$$a = a^{IDEAL} + a^{MONO} + a^{CHAIN} \tag{A1}$$

and for SW chain molecules with potential parameters $K\epsilon$ and λ, we have the following specific expressions:[53,54,56–59]

1. Ideal contribution, $a^{IDEAL} = \ln(\eta)$, where $\eta = 3\rho^*$.
2. Monomers contribution,

$$a^{MONO} = 3(a^{HS} + \beta a_1 + \beta^2 a_2), \tag{A2}$$

where

$$a^{HS} = \frac{4\eta - 3\eta^2}{(1-\eta)^2}, \tag{A3}$$

$$a_1 = \left(\frac{2+\sqrt{K}}{3}\right)^2 a_1^{sw-sw}, \tag{A4}$$

$$a_2 = \left(\frac{2+K}{3}\right)^2 \frac{1}{2}\epsilon K^{HS}\eta\frac{\partial}{\partial\eta}a_1^{sw-sw}, \tag{A5}$$

and

$$a_1^{sw-sw} = -4\eta(\lambda^3 - 1)\epsilon g^{HS}[\sigma, \eta^{eff}]. \tag{A6}$$

The expressions for $g[\sigma, \eta^{eff}]$, η^{eff} and K^{HS} are given in Refs. 53 and 54.

3. The Chain contribution is

$$a^{CHAIN} = -\ln y_{sw-sw} - \ln y_{hs-sw}, \tag{A7}$$

where the cavity functions for the SW-SW and HS-SW bonds are given in Refs. 53 and 54. The energy-depth potentials ϵ and $\sqrt{K}\epsilon$ are used for the SW-SW and HS-SW interactions, respectively.

To compute liquid-vapor equilibrium, the thermodynamic equilibrium conditions are required, $T^v = T^l$,

$P^v = T^l$, and $\mu^v = \mu^l$, where v and l denote vapor and liquid phases. The chemical potential and pressure are obtained using Eq. (A1) and the thermodynamic relations

$$\mu = \left(\frac{\partial A}{\partial N}\right)_{T,V} = a + \eta\left(\frac{\partial a}{\partial \eta}\right)_{T,V}, \tag{A8}$$

and

$$Z = \frac{P}{Nk_BT} = \eta\left(\frac{\partial a}{\partial \eta}\right)_{T,V}, \tag{A9}$$

where Z is the compressibility factor.

[1] Y. S. Velichko, S. I. Stupp, and M. O. de la Cruz, J. Phys. Chem. B **112**, 2326 (2008).
[2] C. Avendaño, A. Gil-Villegas, and E. González-Tovar, Chem. Phys. Lett. **470**, 67 (2009).
[3] A. J. Crane, F. J. Martínez-Veracoechea, F. A. Escobedo, and E. A. Müller, Soft Matter **4**, 1820 (2008).
[4] M. Sammalkorpi, S. Sanders, A. Z. Panagiotopoulos, M. Karttunen, and M. Haataja, J. Phys. Chem. B **115**, 1403 (2011).
[5] S. V. Burov and A. K. Shchekin, J. Chem. Phys. **133**, 244109 (2010).
[6] C. McBride and C. Vega, J. Chem. Phys. **117**, 10370 (2002).
[7] C. McBride, C. Vega, and L. G. MacDowell, Phys. Rev. E **64**, 011703 (2001).
[8] S. Puvvada and D. Blankschtein, J. Chem. Phys. **92**, 3710 (1990).
[9] G. Foffi, C. De Michele, F. Sciortino, and P. Tartaglia, J. Chem. Phys. **122**, 224903 (2005).
[10] A. Jusufi, A.-P. Hynninen, and A. Z. Panagiotopoulos, J. Phys. Chem. B **112**, 13783 (2008).
[11] A. T. Bernardes, V. B. Henriques, and P. M. Bisch, J. Chem. Phys. **101**, 645 (1994).
[12] Z. Wang and R. G. Larson, J. Phys. Chem. B **113**, 13697 (2009).
[13] S. J. Marrink, D. P. Tieleman, and A. E. Mark, J. Phys. Chem. B **104**, 12165 (2000).
[14] J. L. Woodhead and C. K. Hall, Langmuir **26**, 15135 (2010).
[15] B. C. Stephenson, K. J. Beers, and D. Blankschtein, J. Phys. Chem. B **111**, 1063 (2007).
[16] R. Pool and P. G. Bolhuis, Phys. Chem. Chem. Phys. **8**, 941 (2006).
[17] L. Vega, E. de Miguel, L. F. Rull, G. Jackson, and I. A. McLure, J. Chem. Phys. **96**, 2296 (1992).
[18] A. Giacometti, G. Pastore, and F. Lado, Mol. Phys. **107**, 555 (2009).
[19] S. V. Fridrikh and J. E. G. Lipson, J. Chem. Phys. **116**, 8483 (2002).
[20] A. P. Malanoski and P. A. Monson, J. Chem. Phys. **107**, 6899 (1997).
[21] R. G. Larson, J. Chem. Phys. **91**, 2479 (1989).
[22] J. Huang, Y. Wang, and C. Qian, J. Chem. Phys. **131**, 234902 (2009).
[23] S. Fujiwara, T. Itoh, M. Hashimoto, and R. Horiuchi, J. Chem. Phys. **130**, 144901 (2009).
[24] D. Bedrov, G. D. Smith, K. F. Freed, and J. Dudowicz, J. Chem. Phys. **116**, 4765 (2002).
[25] S. Tsonchev, G. C. Schatz, and M. A. Ratner, J. Phys. Chem. B **108**, 8817 (2004).
[26] G. K. Bourov and A. Bhattacharya, J. Chem. Phys. **122**, 044702 (2005).
[27] G. Brannigan, Phys. Rev. E **72**, 011915 (2005).
[28] T. Zehl, M. Wahab, H.-J. Mögel, and P. Schiller, Langmuir **22**, 2523 (2006).
[29] T. Zehl, M. Wahab, H.-J. Mögel, and P. Schiller, Langmuir **25**, 7313 (2009).
[30] F. Romano and F. Sciortino, Nature Mater. **10**, 171 (2011).
[31] E. Zaccarelli, S. V. Buldyrev, E. La Nave, A. J. Moreno, Saika-Voivod, F. Sciortino, and P. Tartaglia, Phys. Rev. Lett. **94**, 218301 (2005).
[32] E. Bianchi, J. largo, P. Tartaglia, E. Zaccarelli, and F. Sciortino, Phys. Rev. Lett. **97**, 168301 (2006).
[33] F. Sciortino, Eur. Phys. J. B **64**, 505 (2008).
[34] R. P. Sear, S. Chung, G. Markovich, W. M. Gelbart, and J. R. Heath, Phys. Rev. E **59**, R6255 (1999).
[35] S. Mejía-Rosales, A. Gil-Villegas, B. Ivlev, and J. Ruíz-García, J. Phys.: Condens. Matter **14**, 4795 (2002).
[36] S. Mejía-Rosales, A. Gil-Villegas, B. Ivlev, and J. Ruíz-García, J. Phys. Chem. B **110**, 22230 (2006).
[37] K.-H. Roh and D. C. Martin, J. Lahann, Nature Mater. **4**, 759 (2005).
[38] A. Walther and A. H. E. Müller, Soft Matter **4**, 663 (2008).
[39] B. J. Park, C.-H Choi, S.-M. Kang, K. E. Tettey, C.-S. Lee, and D. Lee, Langmuir **29**, 1841 (2013).
[40] A. Walther and A. H. E. Müller, Chem. Rev. **113**, 5194 (2013).
[41] F. Sciortino, A. Giacometti, and G. Pastore, Phys. Rev. Lett. **103**, 237801 (2009).
[42] S. Salaniwal, S. K. Kumar, and A. Z. Panagiotopoulos, Langmuir **19**, 5164 (2003).
[43] A. D. Mackie, K. Onur, and A. Z. Panagiotopoulos, J. Chem. Phys. **104**, 3718 (1996).
[44] A. D. Mackie and A. Z. Panagiotopoulos, Langmuir **13**, 5022 (1997).
[45] M. A. Floriano, E. Caponetti, and A. Z. Panagiotopoulos, Langmuir **15**, 3143 (1999).
[46] J. S. Rowlinson and F. L. Swinton, *Liquids and Liquid Mixtures*, 3rd ed. (Butterworth Scientific, London, UK, 1982).
[47] G. Jiménez-Serratos, C. Vega, and A. Gil-Villegas, J. Chem. Phys. **137**, 204104 (2012).
[48] J. W. Cahn and J. E. Hilliard, J. Chem. Phys. **28**, 258 (1958).
[49] W. H. Press, S. A. Teukolsky, W. T. Vetterling, and B. P. Flannery, *Numerical Recipes in Fortran 90*, 2nd ed. (Cambridge University Press, Cambridge, UK, 1996).
[50] E. de Miguel and G. Jackson, J. Chem. Phys. **125**, 164109 (2006).
[51] E. de Miguel, J. Phys. Chem. B **112**, 4674 (2008).
[52] P. E. Brumby, A. J. Haslam, E. de Miguel, and G. Jackson, Mol. Phys. **109**, 169 (2011).
[53] A. Gil-Villegas, A. Galindo, P. J. Whitehead, S. J. Mills, G. Jackson, and A. N. Burgess, J. Chem. Phys. **106**, 4168 (1997).
[54] A. Galindo, L. A. Davies, A. Gil-Villegas, and G. Jackson, Mol. Phys. **93**, 241 (1998).
[55] M. S. Wertheim, J. Stat. Phys. **35**, 19 (1984); **35**, 35 (1984); **42**, 459 (1986); **42**, 477 (1986); J. Chem. Phys. **85**, 2929 (1986); **87**, 7323 (1987).
[56] Y. Peng, H. Zhao, and C. McCabe, Mol. Phys. **104**, 571 (2006).
[57] M. C. dos Ramos and F. J. Blas, Mol. Phys. **105**, 1319 (2007).
[58] P. Morgado, H. Zhao, F. J. Blas, C. McCabe, L. P. N. Rebelo, and E. J. M. Filipe, J. Phys. Chem. B **111**, 2856 (2007).
[59] P. Morgado, R. Tomás, H. Zhao, M. C. dos Ramos, F. J. Blas, C. McCabe, and E. J. M. Filipe, J. Phys. Chem. C **111**, 15962 (2007).
[60] F. Sciortino, Nature Mater. **1**, 145 (2002).
[61] G. Foffi, E. Zaccarelli, S. Buldyrev, F. Sciortino, and P. Tartaglia, J. Chem. Phys. **120**, 8824 (2004).
[62] J. C. F. Toledano, F. Sciortino, and E. Zaccarelli, Soft Matter **5**, 2390 (2009).
[63] D. Frenkel and B. Smit, *Understanding Molecular Simulation* (Academic Press, London, 2002).
[64] C. Valeriani, P. J. Camp, J. W. Zwaninkken, R. van Roij, and M. Dijkstra, J. Phys.: Condens. Matter **22**, 104112 (2010).
[65] V. Kapila, J. M. Harris, P. A. Deymier, and S. Raghavan, Langmuir **18**, 3728 (2002).